



https://doi.org/10.1016/j.ultrasmedbio.2020.11.019

Original Contribution

EXPERIMENTAL AND COMPUTATIONAL INVESTIGATION OF GUIDED WAVES IN A HUMAN SKULL

CHRISTOPHER SUGINO,* MASSIMO RUZZENE,† and ALPER ERTURK*

*G. W. Woodruff School of Mechanical Engineering, Georgia Institute of Technology, Atlanta, Georgia, USA; and † Department of Mechanical Engineering, University of Colorado Boulder, Boulder, Colorado, USA

(Received 17 June 2020; revised 14 November 2020; in final from 17 November 2020)

Abstract—We investigate guided (Lamb) waves in a human cadaver skull through experiments and computational simulations. Ultrasonic wedge transducers and scanning laser Doppler vibrometry are used respectively to excite and measure Lamb waves propagating in the cranial bone of a degassed skull. Measurements are performed over a section of the parietal bone and temporal bone spanning the squamous suture. The experimental data are analyzed for the identification of wave modes and the characterization of dispersion properties. In the parietal bone, for instance, the A₀ wave mode is excited between 200 and 600 kHz, and higher-order Lamb waves are excited from 1 to 1.8 MHz. From the experimental dispersion curves and average thickness extracted from the skull computed tomography scan, we estimate average isotropic material properties that capture the essential dispersion characteristics using a semi-analytical finite-element model. We also explore the leaky and non-leaky wave behavior of the degassed skull with water loading in the cranial cavity. Successful excitation of leaky Lamb waves is confirmed (for higher-order wave modes with phase velocity faster than the speed of sound in water) from 500 kHz to 1.5 MHz, which may find applications in imaging and therapeutics at the brain periphery or skull-brain interface (e.g., for metastases). The non-leaky A₀ Lamb wave mode propagates between 200 and 600 kHz, with or without fluid loading, for potential use in skull-related diagnostics and imaging (e.g., for sutures). (E-mail: csugino3@gatech.edu) © 2020 World Federation for Ultrasound in Medicine & Biology. All rights reserved.

Key Words: Lamb waves, Human skull, Scanning laser Doppler vibrometry.

INTRODUCTION

Having wide applicability to the treatment and prevention of skull and brain injury or disorder, the biomechanics of human cranial bone have been studied extensively (Yoganandan et al. 1995; Margulies and Thibault 2000). Researchers have characterized the mechanical/acoustical properties and microstructure of cranial bone using a variety of techniques, ranging from fundamental material testing studies (McElhaney et al. 1970; Hubbard 1971; Wood 1971; Jaslow 1990; Peterson and Dechow 2003) to acoustic measurements (Fry and Barger 1978) and computational studies using microcomputed tomography (Boruah et al. 2017). More recently, the rapid growth of research in focused ultrasound (FUS) therapeutic techniques for the brain (Lipsman et al. 2014; Aubry and Tanter 2016) has led to

a renewed interest in the study of the acoustic and structural properties of the skull. FUS has been used for targeted blood—brain barrier disruption (Mesiwala et al. 2002; Hynynen et al. 2005; Kinoshita et al. 2006) and has been used successfully to treat essential tremor in humans *via* non-invasive thalamotomy (Elias et al. 2013, 2016).

Current medical ultrasound techniques for the brain rely on normal-incidence ultrasound using a hemispherical phased array (Clement et al. 2000; Hynynen et al. 2004), resulting in significant efficiency loss and heating in the skull because of impedance mismatch and internal reflections. To achieve sufficient localized ultrasonic energy in the brain, the phased array must correct for the aberration at the skull interface (Kyriakou et al. 2014), relying on computed tomography (CT) scans of the skull (Clement and Hynynen 2002; Aubry et al. 2003). However, because of the geometry of the hemispherical phased array and reliance on normal-incidence ultrasound, current FUS devices can focus ultrasound only at the central

Address correspondence to: Christopher Sugino, Mechanical Engineering, Georgia Institute of Technology, 801 Ferst Drive, Atlanta, GA 30332, USA. E-mail: csugino3@gatech.edu

region of the brain (Odeen et al. 2014), greatly limiting their potential therapeutic applications. For instance, while focusing ultrasound on the central region of the brain is of value for certain therapeutic applications mentioned previously (e.g., thalamotomy for essential tremor), tumors around the brain periphery cannot be accessed without excessive skull heating (Odeen et al. 2014). To address this shortcoming, Firouzi et al. (2017) proposed the use of an array of wedge transducers and mode conversion to enhance ultrasound transmission in the brain, illustrating improved transmission through a submerged skull fragment and reduced heating in the skull in simulations. Although this technique promises an enhancement of the accessible region of the brain via Lamb waves and mode conversion, implementations will likely rely heavily on the understanding and the characterization of guided wave propagation in the human skull. Furthermore, guided waves have many potential applications in the human skull beyond mode conversion-based FUS because they are sensitive to bone geometry (Moilanen et al. 2007), material properties (Nicholson et al. 2002; Bochud et al. 2017) and the properties of the adjacent medium (Vavva et al. 2008) (e.g., hemorrhage around the brain periphery). For example, non-leaky guided waves could potentially be used to detect craniosynostosis (Regelsberger et al. 2006; Fearon et al. 2007) (i.e., premature bone fusing in infant skulls) or skull fracture (Weinberg et al. 2010; Rabiner et al. 2013) without the need for full CT scans.

Similar diagnostic and bone-monitoring strategies leveraging guided waves have been extensively investigated in human long bones (Moilanen 2008), which act as mechanical waveguides. Nicholson et al. (2002) piloted the use of guided waves to enhance ultrasonic inspection of long bones, leveraging the fact that guided wave dispersion is sensitive to thickness and material property variation. Protopappas et al. (2006) developed a model for guided waves propagating in healing bone, suggesting that guided waves could be used to monitor bone healing. Guided waves have also been used to measure cortical bone thickness (Moilanen et al. 2007) and bone properties (Foiret et al. 2014; Bochud et al. 2017). Unlike such sections of long bone, human skull bone is highly non-uniform in both structure and material properties, lacking the orientation of long consistent material (Peterson and Dechow 2003). Previous investigations on Lamb wave propagation include the work of Estrada et al. (2018), which presented measured guided waves in fully immersed cranial bone using laser excitation and near-field pressure measurements. Similar numerical studies were described by Adams et al. (2017), who considered the use of a concave phased array to excite and measure Lamb waves in the skull, using farfield measurements to observe guided waves. However, significant experimental challenges remain in terms of the

ability to extract distinct dispersion branches for guided waves in the human skull, suggesting that additional investigations need to be conducted to achieve full characterization of multimodal propagation in the skull.

In the work described here, we performed direct velocity measurement of guided waves propagating in a degassed human cadaver skull. Ultrasonic transducers of the type commonly used for non-destructive evaluation (NDE) were used together with scanning laser Doppler vibrometry to measure guided waves propagating in cranial bone. Experiments were performed both with and without fluid loading inside the skull cavity, providing insight into which guided wave modes of the skull are leaky (and, hence, useful for mode conversion-based ultrasound) and which are non-leaky, capable of propagating over long distances in the skull. CT scans of the geometry of the skull enabled the creation of finite-element models that accurately capture the skull cross-section along the scan line, up to the precision of the CT scan $(0.44 \times 0.44$ -mm pixels within each slice, 0.5-mm slice thickness). In addition, Lamb wave dispersion properties of the skull were estimated using a semi-analytical finite-element (SAFE) model, which provides the framework for the estimation of average geometric and material properties that can be used to analyze leaky and non-leaky wave behavior in the skull.

METHODS

Established techniques to estimate multimode dispersion curves from experimental data include the 2-D fast Fourier transform (FFT) (Alleyne and Cawley 1991) and time-frequency analyses (Niethammer et al. 2001). More recently, 2-D FFT dispersion estimations have grown in popularity by taking advantage of the spatial resolution provided by scanning laser Doppler vibrometers (SLDVs), which enable non-contact measurements velocity wavefields (Ruzzene full 2007; Michaels et al. 2011; Tian and Yu 2014). In this work, 1-D velocity line scans were performed using a Polytec PSV-500 SLDV and processed using the 2-D FFT technique. The SLDV conducts surface velocity measurements on a prescribed set of spatial points by repeating the excitation and measuring the response at each scan point, using a digital trigger to maintain consistent synchronization between measurements (see Fig. 1). In this work, measurements were performed at 7.8125 MHz with 0.24 and 0.15 mm between each measurement point for the temporal and parietal scans, respectively.

The scan yields measurements of the velocity field v = v(x,t), where x and t are the spatial and temporal sample points, respectively. These data are then processed using the 2-D FFT, which yields the spectral representation $V = V(k, \omega)$ of the wavefield, where k and ω are the

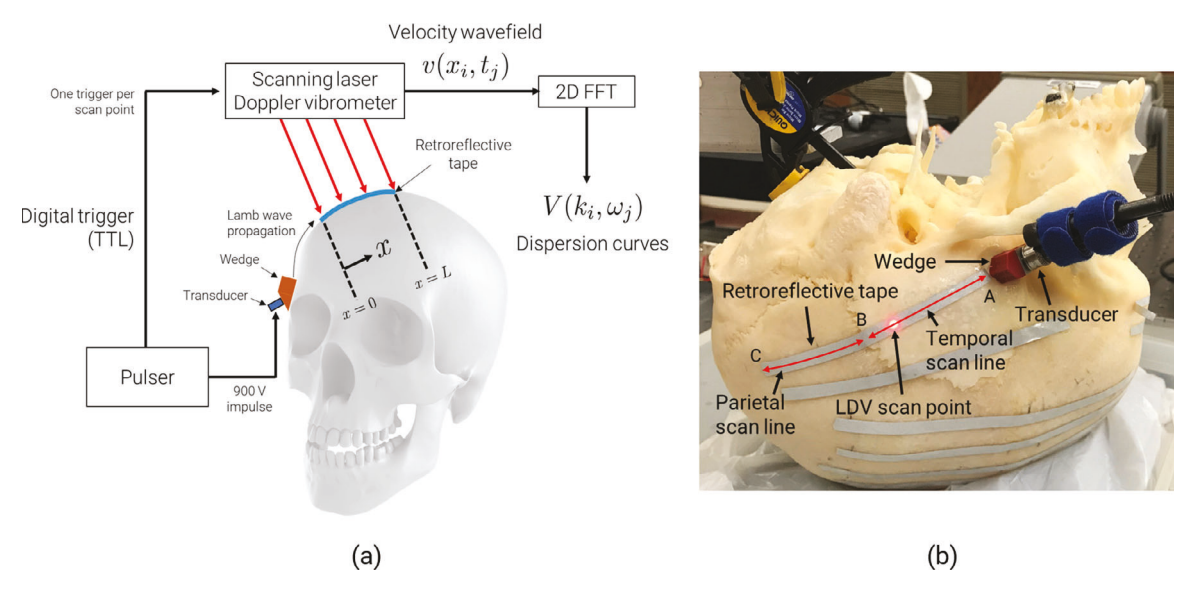


Fig. 1. (a) Schematic of the experimental approach for measuring the wavefield and calculating the dispersion relations of Lamb waves propagating in the human skull. (b) Close-up view of experimental setup, highlighting the two scan lines used in this study. The temporal scan line goes from A to B, while the parietal scan line goes from C to B. (FFT = fast Fourier transform; LDV = laser Doppler vibrometer; TTL = transistor-transistor logic).

wavenumber (rad/m) and angular frequency (rad/s), respectively. The magnitude of the 2-D spectrum $|V(k,\omega)|$ provides a representation of the wavefield in the frequency-wavenumber domain. This procedure is illustrated schematically in Figure 1. Specifically, the corresponding surface highlights regions of concentration of the frequency/wavenumber content, which effectively outline the dispersion branches of the propagation medium within the frequency range of excitation. Broadband excitation thus allows the experimental identification of the dispersion branches and enables their subsequent analysis and characterization, which is here assisted by numerically estimated dispersion curves.

Numerous strategies for modeling the dispersion of guided waves in waveguides of arbitrary cross-section can be found in the literature. Here, we use the SAFE formulation first introduced by Datta et al. (1988), which casts the propagation problem as an eigenvalue problem through the finite-element discretization of the thickness of waveguides of uniform cross-section. This technique allows the analysis of layered structures with arbitrary elastic properties and was employed here to model the skull cross-section as an equivalent isotropic layer of constant thickness bounded by air. For the SAFE results described here, 50 elements were used for discretization through the thickness of the bone to capture high-order Lamb wave modes accurately. The predictions from SAFE support the interpretation of the experimentally observed dispersion curves, the identification of leading wave modes (symmetric S, anti-symmetric A) and the estimation of averaged mechanical properties that provide the

best fit to the experimental data. For these SAFE dispersion calculations, it is necessary only to specify the thickness, longitudinal wave speed and shear wave speed of the medium. To obtain the associated isotropic elastic properties (e.g., Young's modulus and Poisson's ratio), it is necessary to specify the density of the medium. For the purpose of this work, the isotropic elastic properties were obtained by assuming an average bone density value (McElhaney et al. 1970), providing a baseline for comparison with other reported elastic constants for the skull. The use of an average bone density introduces significant uncertainty in the Young's modulus of the medium; however, the measurement of isotropic mechanical properties is not the main focus of this work. Our ongoing and parallel body of work uses three-layer modeling of the cortical tables and the diploë for more advanced mechanical identification parameter from wave propagation (Mazzoti et al., under review) and vibration (Kohtanen et al., in preparation) experiments.

Guided waves propagating faster than the speed of sound in an adjacent fluid medium radiate energy into the fluid domain at an angle based on Snell's law (Dayal and Kinra 1989). As such, it is expected that these "leaky" wave modes will be attenuated significantly in the skull as they lose energy to the fluid domain, whereas non-leaky wave modes will propagate without significant attenuation. To predict which experimentally measured wave modes could potentially leak energy into the cranial cavity, it is convenient to convert the previously presented frequency-wavenumber data to velocity-frequency data using the relationship $\nu_p = \omega/k$, where ν_p is the phase

velocity of the wave mode with frequency ω and wavenumber k. With this conversion, the speed of sound in water becomes a horizontal line (corresponding to constant phase velocity), and the frequency/wavenumber spectral data is separated into leaky modes (above the sound line) and non-leaky modes (below the sound line).

Dry human cadaver skulls were obtained from Skulls Unlimited Inc. (Oklahoma City, OK, USA). For this work, the skull of a 64-y-old Caucasian man was degassed for 48 h in de-ionized water, then stored in a 10% neutral buffered formalin solution (Fry and Barger 1978). This degassing process serves to remove trapped air from within the cranial bone; however, experiments were performed in air, creating the possibility for re-gassing during experiments. For this reason, the skull was removed from the formalin solution only during active testing and was stored immediately once scans were completed. Screw-in ultrasonic transducers (Olympus C546-SM) with a center frequency of 3.5 MHz and diameter of 6.35 mm were used together with a 45° wedge (Olympus Accupath) to excite guided waves in the skull. The transducer was selected as a tradeoff between its size and center frequency. Transducers with lower center frequencies require larger piezoelectric elements and wider cross-section, limiting the wavelengths of guided waves that can be excited and preventing good contact between the wedge and skull surface. To maintain effective transmission through the wedge and skull surface, ultrasonic coupling gel (Olympus Couplant D) was used at the interface between the transducer and wedge, as well as between the wedge and surface of the skull. Because of the uneven surface of the skull, it is beneficial to use a small transducer to minimize the additional phase variation for the incident wave. The transducer and wedge were held against the skull surface using an adjustable three-linkage mounting arm, allowing the transducer to be angled and placed freely on the surface. The skull was held in place with a C-clamp placed through the foramen magnum onto the occipital bone, and was supported by soft foam to reduce the potential for wave reflections. Waves were excited far from both held surfaces, such that the effect of clamping could be neglected. The input to the transducer was generated with a high-voltage pulser-receiver (Panametrics 5058 PR) operating at 900 V, creating a broadband incident wave. To improve the data quality of laser Doppler vibrometer velocity measurements, retroreflective tape was applied along each scan line. This surface treatment using retroreflective tape is required to increase the amount of light reflected from the skull back to the laser head, greatly increasing the signal-to-noise ratio (SNR). This type of surface treatment would be undesirable for clinical systems or future in vivo studies; however, SLDV systems are available that use a near-infrared laser (1550-nm wavelength), which has been used successfully for ultrasonic measurements in vivo on the surface of human skin surface

while maintaining maximum permissible exposure limits (Zhang et al. 2019). Because only a single LDV head was used, only the velocity component in the direction of the laser beam was measured. The experimental setup is illustrated in Figure 1.

Results are here presented for a line scan that spans the squamous suture, going from one of the thinnest sections of the temporal bone to the parietal bone (see Fig. 1). To obtain the geometry of the skull along the examined scan line, CT scans of the full skull were performed at Emory University using a Siemens SOMATOM Force Dual Source CT Scanner at 120 kV and 462 mA with a pixel size of 0.44×0.44 mm and slice thickness of 0.5 mm, using reconstruction kernel Qr69. These scans were imported into the software Materialise Mimics and then re-sliced along the scan line to obtain the cross-section of the skull in the plane of the scan line. Once the resliced image of the skull was obtained, the boundaries of the image were used to calculate the thickness along the scan line. This calculation yields the average thickness of each scan line, which is used in the simplified SAFE dispersion model. The thickness profile also quantifies the amount of thickness variation in each scan line, which can dramatically affect the propagation of guided waves. This procedure is illustrated in Figure 2.

The CT scan cross-section of the scan line is provided in Figure 2b, and the corresponding thickness profile in Figure 2c. Thickness is estimated as the minimum distance between the interior and exterior boundaries in the scan section. As shown near point B in Figure 2b, the squamous suture forms a narrow gap that spans the entire bone thickness at a sharp angle, which is expected to cause significant reflections. As such, the wedge excitation for both measurements was oriented toward the squamous suture, avoiding reflections at the suture interface until the end of the scan line. According to the notation of Figure 2, the temporal and parietal scan lines are referred to as AB and CB, respectively. It should be noted that the resolution of the CT scan $(0.44 \times 0.44 \times 0.5 \text{ mm})$ introduces some uncertainty into the predictions of the SAFE dispersion model. In dimensionless form, Lamb wave dispersion curves relate normalized wave speed to normalized frequency-thickness product. As such, varying the thickness parameter in the model has the effect of stretching the frequency axis of the SAFE dispersion model. In this way, dispersion predictions based on the thickness of skull bone at a single point would be significantly uncertain, especially at the thinnest section of the bone. However, the use of average thickness computed over a long section of the skull bone has the effect of reducing the uncertainty caused by the CT scan resolution. We can approximate this uncertainty by assuming a worst-case error of 0.5 mm (the slice thickness of the CT scan) for the N image points used in the average thickness calculation of each scan line, giving

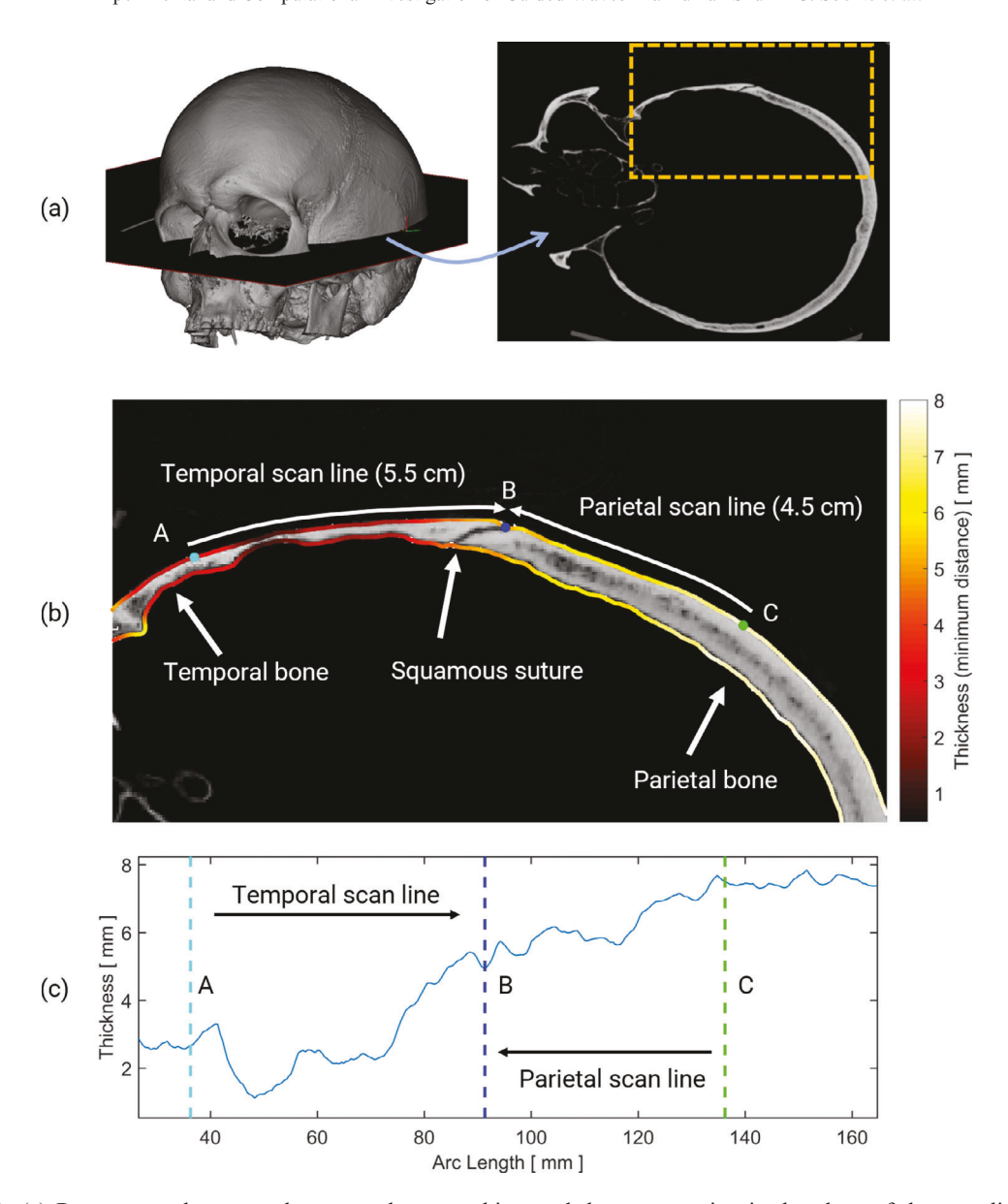


Fig. 2. (a) Reconstructed computed tomography scan object and the cross-section in the plane of the scan line. (b) Zoomed-in view of the boxed region in (a) highlighting the scan lines as illustrated in Figure 1 and their thickness variation. (c) Computed thickness as a function of arc length. Excitation for the temporal scans was performed from A to B, whereas excitation for the parietal scan was performed from C to B, such that both scans terminated at the squamous suture.

an approximate uncertainty in the mean of 0.5 mm/ \sqrt{N} . Line AB comprised 123 points of the CT scan with average thickness 2.9 mm, while line CB comprised 96 points with average thickness 6.2 mm, yielding uncertainties of 0.045 and 0.051 mm, respectively. This corresponds to 1.5% and 0.8% uncertainty in the mean thickness for lines AB and CB, respectively, indicating the same uncertainty in the wavenumber of a given wave mode in the SAFE dispersion model.

The CT scans of the skull are also useful for numerical simulations using the finite-element method. Finite-element

simulations were performed using the commercial software COMSOL Multiphysics. These 2-D simulations used plane-strain linear elastic governing equations for the bone regions and pressure acoustics in the fluid domain inside the skull, with fluid-structure coupling at the interface. To highlight both leaky and non-leaky wave behavior, transient simulations were performed with 10 cycle Gaussian sine bursts at 50 and 200 kHz. These simulations are valuable for improved visualization of guided wave propagation and the corresponding leaky wave radiation into the fluid. As the finite-element model based on full-skull CT scan has a

cross-section of homogeneous composition (*i.e.*, no porous structure), only the non-idealities caused by curvature and non-uniform thickness are included in the simulations (future efforts will include diploë structure based on micro-CT scan). The mesh size was selected to maintain seven elements per wavelength for the slowest guided wave mode at the center frequency of excitation. Correspondingly, a fixed time step satisfying the Courant—Friedrichs—Lewy (CFL) condition with a Courant number of 0.5 (based on the longitudinal wave speed in bone) was used.

RESULTS

Experimental wave dispersion

The experimental velocity field v(x,t), the magnitude of the frequency/wavenumber spectrum $|V(k,\omega)|$ and the analytical dispersion curves for line CB are illustrated in Figure 3. The raw velocity space-time wavefield data v(x,t) in Figure 3a reveal that the scan line was

sufficiently long to capture propagating wave modes without significant reflections. The reduction in velocity amplitude as the waves propagate away from the excitation suggests that the system exhibits significant attenuation. The plot highlights the presence of several wave modes propagating at different speeds, which makes their identification challenging. There is a distinct fast wave that propagates for approximately 2 cm and appears mostly non-dispersive, in addition to other wave components that exhibit different levels of dispersion. The representation in the frequency/wavenumber domain in Figure 3b, which depicts $|V(k,\omega)|$ as a colormap in logarithmic scale, helps the analysis of the wavefield and the identification of the main wave modes. This is further supported by the SAFE dispersion curves, which are superimposed on the colormap of Figure 3b as black solid lines. SAFE computations are here conducted by using the average thickness of line CB (6.2 mm) (see Fig. 2) and isotropic properties for a single layer

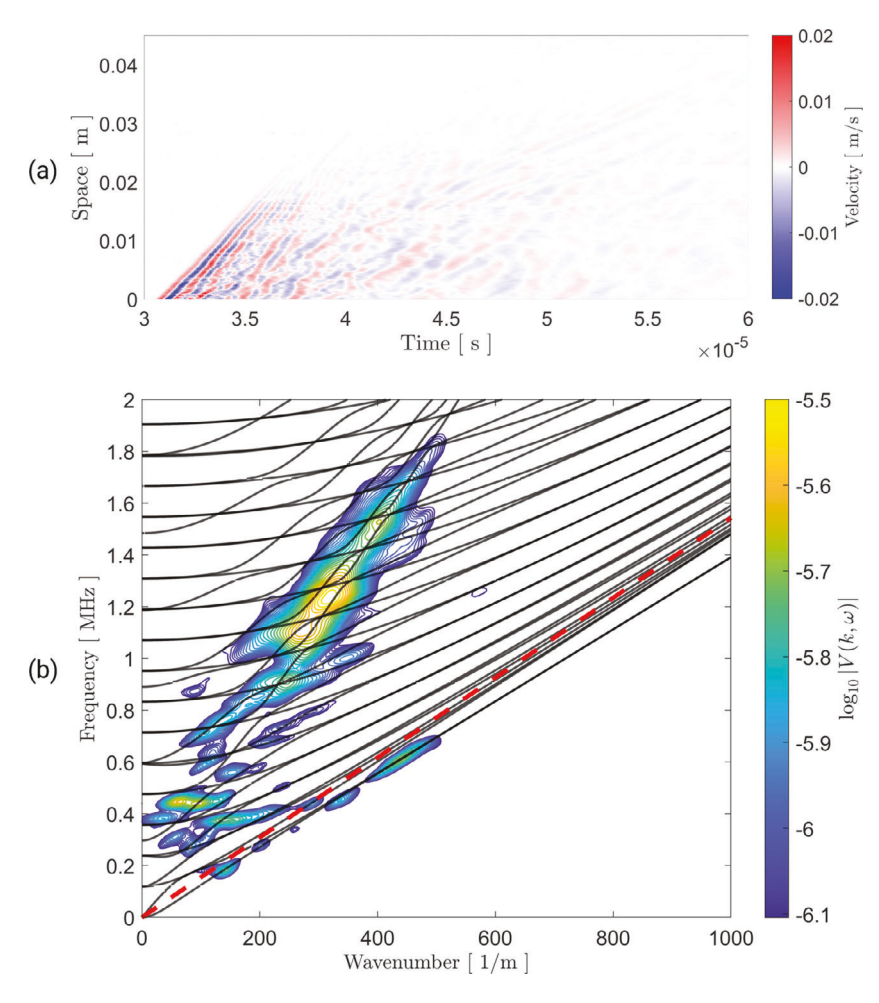


Fig. 3. (a) Experimental velocity data versus space and time. (b) Spectral data $|V(k,\omega)|$ obtained using the 2-D fast Fourier transform FFT (contours) and semi-analytical dispersion curves (*solid black lines*) for line CB. The material properties and thickness for the semi-analytical finite-element (SAFE) dispersion model are listed in Table 1. The *red dashed line* marks the dispersion curve of sound waves in water.

structure corresponding to longitudinal and shear wave speeds of 3680 m/s and 1475 m/s, which are estimated using the slope of the fast (between 800 kHz and 1.6 MHz) and slow (between 200 and 600 kHz) wave branches in the experimental spectral data of Figure 3b. Superposition of the numerical dispersion curves on the frequency/wavenumber spectrum of the experimental wavefield reveals that description of guided waves through this simplified set of properties provides a good representation of the dispersion characteristics in the considered frequency range. The colormap exhibits a cluster of modes above 800 kHz, which mostly concentrate along the longitudinal wave line of the spectrum. In addition, one can observe that the lowest mode, which matches the lowest anti-symmetric mode A_0 branch of the numerical dispersion, is excited up to a frequency of 700 kHz. This mode propagates slower than the speed of sound in water, whose dispersion curve is represented by

a dashed red line in Figure 3b, across the entire dispersion branch, which suggests that this mode may not leak in a coupled water environment. In contrast, all other modes, and in particular the modal cluster above 800 kHz, appear above the sound line and may therefore be of the leaky type.

Similar experiments were performed in the temporal bone (line AB) on the opposite side of the squamous suture. Results are illustrated in Figure 4. The experimental velocity wavefield in Figure 4a indicates that although energy propagates through the scanned region, the separate propagating wave modes are not easily identifiable (as in Fig. 3a). Furthermore, it is clear that the wave energy is greatly diminished after approximately 1 cm of propagation, suggesting that waves are reflecting and/or scattering at an interface. This experimental observation aligns with the CT scan data of Figure 2, which indicates that the thickness changes from 2.7 mm at point A to the

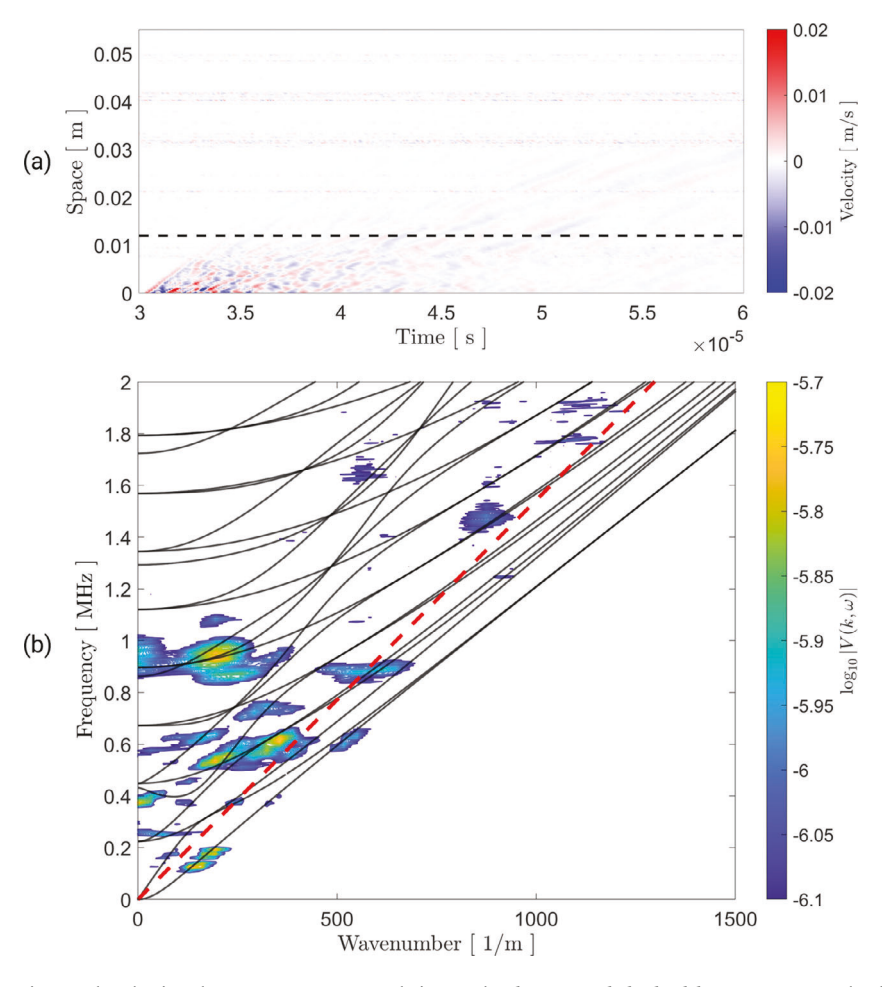


Fig. 4. (a) Experimental velocity data versus space and time. The *horizontal dashed line* represents the location of the minimum thickness in this scan line. (b) Spectral data $|V(k,\omega)|$ obtained using the 2-D fast Fourier transform (contours) and semi-analytical finite-element (SAFE) dispersion curves (*solid black lines*) for line AB. The material properties and thickness for the SAFE dispersion model are listed in Table 1. The *red dashed line* marks the dispersion curve of sound waves in water.

minimum thickness of 1.1 mm after a distance of 1.2 cm. For reference, the location of minimum thickness is represented by the dashed line in Figure 4a.

Ultrasound in Medicine & Biology

In general, this section of the temporal bone has significant thickness variation, ranging in thickness from 1.1-5.4 mm (see Fig. 2), corresponding to nearly a factor of 5 change in both the wavelength and frequency of a given Lamb wave mode. This variation makes it challenging to identify distinct wave modes, and the measured waves are likely only representative of the skull bone near the excitation at point A. The slowest Lamb wave mode (A_0) is captured effectively up to 600 kHz despite the significant thickness variation, likely because it has a relatively long wavelength and hence is less sensitive to sudden changes in thickness. At high frequencies, the dispersion of the A_0 wave mode depends primarily on the shear wave velocity (i.e., it approaches the Rayleigh wave dispersion curve), such that the data in Figure 4 can be used to estimate the shear wave velocity in section AB. Use of the average thickness of 2.9 mm (computed from the CT scan geometry) and a shear wave velocity of 1300 m/s matches the slope of the slowest wave mode (\underline{A}_0 , *i.e.*, the mode with greatest wavenumber at a given frequency) in the SAFE results to the slope observed in the experimental data between 200 and 600 kHz in Figure 4b. Because most of the remaining wave energy is reflected or scattered after the first 1 cm of propagation, the experimental dispersion lacks wave modes that can be used to identify the longitudinal wave speed. For concreteness, SAFE dispersion curves are shown for $c_1 = 2500$ m/s. The material properties used for the SAFE dispersion results of the two scan lines are summarized in Table 1. Because the SAFE dispersion simulations rely on a homogenized cross-section and average thickness, the slight variation in bone properties in Table 1 can be attributed to the variation in bone composition in lines AB and CB (see Fig. 2). Additionally, it has been found that the cortical tables of cranial bone have inconsistent material axis alignment (Peterson and Dechow 2003), which may result in further variation in speed of sound.

To define fully the isotropic elastic properties of the material used in the SAFE dispersion calculations, it is necessary to specify the density or Young's modulus of the medium in addition to the velocities given in Table 1.

Table 1. Isotropic properties used for the simplified SAFE dispersion calculations

	Parietal (CB)	Temporal (AB)
Longitudinal wave velocity	3680 m/s	2500 m/s
Shear wave velocity	1475 m/s	1300 m/s
Thickness	6.2 mm	2.9 mm

SAFE = semi-analytical finite element.

The final parameter, Poisson's ratio (for example), depends only on the ratio of longitudinal and shear wave velocities. Because the Young's modulus and density do not directly affect the SAFE dispersion curves, they cannot be identified from the experimental results. Still, these parameters provide a useful baseline for comparison against other reported mechanical properties of cranial bone. For reference, using the average cranial bone density presented by McElhaney et al. (1970) (1410 \pm 526 kg/m³) yields Young's moduli of 6.6 \pm 2.3 GPa for line AB and 8.6 ± 3.2 GPa for line CB. Critically, density plays a role in the prediction of leaky wave radiation because of the interface between bone and fluid. As such, predictive modeling of mode conversion-based ultrasound will depend heavily on accurate estimation of density for thorough CT scan volume estimation and more sophisticated modeling (e.g., three-layer modeling to account for different properties in the cortical tables and the diploë [Mazzoti et al., under review; Kohtanen et al., in preparation]).

Leaky and non-leaky Lamb wave measurements

To investigate the leaky and non-leaky wave phenomena, SLDV experiments were performed with and without fluid loading inside the skull cavity. To maintain consistent excitation for this comparison, scans were first performed after filling the interior of the skull with a water bag, then repeated after emptying the water bag. These results are summarized in Figure 5 for the parietal bone section CB from Figure 2. Although these experiments were performed within minutes of each other, a part of the change observed between Figure 5a and b may be owing to re-gassing of the degassed skull while it was exposed to air. However, it can be expected that the change caused by fluid loading is much more significant than partial re-gassing, especially given the low porosity in the tested region of the skull (Fig. 2b).

The speed of sound in water (denoted by the horizontal red line) separates the results into the leaky and non-leaky regimes. Comparison of Figure 5a and 5b makes it clear that fluid loading results in significant attenuation of leaky wave modes (above the sound line), while the non-leaky wave branches are relatively unaffected. Specifically, the magnitude of the non-leaky wave branch excited at 500 kHz in Figure 5a and 5b is similar because it does not radiate energy into the fluid domain. The large cluster of leaky modes above 800 kHz in Figure 5a is clearly attenuated in Figure 5b, although some energy remains localized along the longitudinal wave speed line.

Finite-element simulations

Numerical finite-element simulations were performed using the same CT scan slice of Figure 2 and the

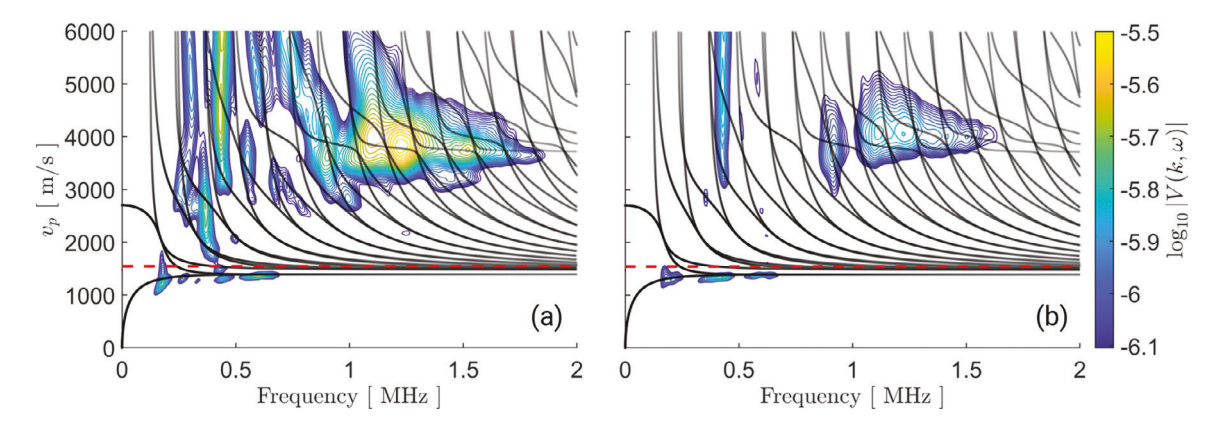


Fig. 5. Velocity magnitude versus frequency for the line CB (a) without fluid loading and (b) with fluid loading. The y-axis and color scale are shared by both figures. The *horizontal dashed line* indicates the speed of sound in water, which separates wave modes into leaky (above the sound line) and non-leaky (below the sound line) regimes. The *black curves* represent the semi-analytical finite-element model dispersion curves for the section CB without fluid loading.

parameters listed in Table 1 for the parietal bone (line CB) and the average bone density of 1410 kg/m^3 from McElhaney et al. (1970). The simulation results for excitation at 50 and 200 kHz are summarized in Figure 6a and 6b, respectively. Animations of the transient simulation results are provided in Supplementary Video 6a and 6b (online only). At a center frequency of 50 kHz, the dominant wave mode excited is the A_0 Lamb wave mode, which is non-leaky. On the other hand, at 200 kHz, multiple guided wave modes are excited in the skull, some of which leak energy into the skull cavity. It

should be noted that these simulation results depend on the arbitrary density selected for the isotropic bone material; however, because the densities of water and bone are similar, the results in Figure 6 are representative of leaky and non-leaky wave behavior.

DISCUSSION

The primary goal of the work described here was to determine whether the use of contact transducers and SLDV can improve the excitation and measurement of

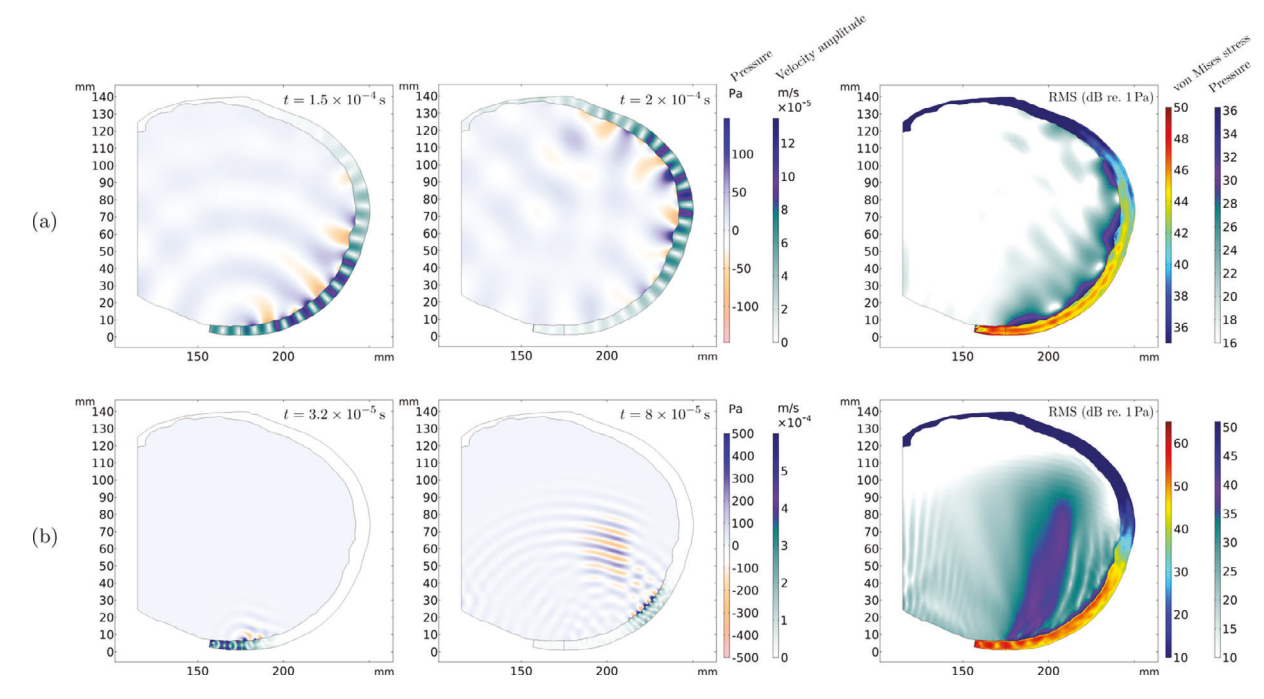


Fig. 6. Transient snapshots and root-mean-square values from finite-element simulations for excitation at (a) 50 kHz and (b) 200 kHz, highlighting non-leaky and leaky wave behaviors, respectively. Animations of transient simulation results for (a) 50 kHz and (b) 200 kHz are available in Supplementary Video 6a and b (online only).

guided waves in the skull. As such, the developed dispersion model (a single, constant-thickness isotropic layer) is greatly simplified compared with the three-layer, highly non-uniform structure of cranial bone. In the specific section of the skull considered (Fig. 2b), there is relatively low porosity, and so it is expected that this type of single-layer model will capture the qualitative dispersion behavior. Future work will focus on further improving the extraction of separate dispersion branches and developing higher-fidelity dispersion models, accounting for anisotropy and layered structure.

These results illustrate that the described experimental technique can provide a direct characterization of leaky and non-leaky wave modes, identifying which guided wave modes may be useful for propagation over long distances and which modes could be used effectively for mode conversion and ultrasound applications in the brain. For example, Figure 5 illustrates that the A_0 wave mode in section CB of the parietal bone is non-leaky and efficiently excited over a wide frequency bandwidth. Leaky Lamb waves can potentially be employed for imaging and therapy in short distances underneath the skull (which is a region not efficiently accessible by bulk compressive waves), while non-leaky waves can find applications in parameter identification as well as imaging and diagnosis within the skull (e.g., for sutures).

Comparison of the results for lines CB and AB (Figs. 3 and 4, respectively) makes it clear that skull geometry plays a vital role in the effective excitation of guided wave modes for use in mode conversion and FUS. In the parietal bone (line CB), multiple leaky wave modes were excited, and the non-leaky A_0 wave mode was excited across a wide frequency range. On the other hand, the significant thickness variation across line AB greatly reduced the ability to excite propagating wave modes, because most of the wave energy was reflected or scattered after only 1.2 cm. As a result, such regions of the skull with significant thickness variation may not be well suited to mode conversion-based FUS, except over very short sections of the bone. On the other hand, these results suggest that such sudden changes in bone geometry may be detectable using guided waves. Such strong dependence on skull geometry complicates the process of aberration correction for mode conversion-based FUS, and there remains a significant need for improved models for fast, predictive dispersion modeling based on measured skull geometry. Recent work in ultrashort-echo-time magnetic resonance imaging (MRI) (Miller et al. 2015) may enable in situ registration of skull geometry within clinical MR-guided focused ultrasound systems, removing the possibility of CT scan misalignment. Future work on mode conversion-based ultrasound should consider the effects of such geometric misalignment, which likely depends on the region of the skull being targeted.

Finite-element simulations provide a useful visualization of leaky and non-leaky guided wave propagation in the skull. The root-mean-square (RMS) pressure field (Fig. 6, right) indicates that non-leaky wave modes generate pressure localized near the skull-fluid interface, whereas leaky wave modes generate directional pressure waves in the fluid. These simulations motivate potential applications for both leaky and non-leaky waves; nonleaky waves are able to propagate over long distances in the skull without significant attenuation caused by fluid loading, whereas leaky waves can be used to send acoustic waves into the skull cavity, especially to access outer regions of the brain or the skull-brain interface. Challenges remain in the realization of near-skull ultrasonic focusing, as the accurate prediction of the pressure field generated by leaky waves requires an accurate model for guided wave propagation in the corresponding section of the skull, which may require a more sophisticated modeling of the skull mechanics and elastodynamics (Mazzoti et al., under review; Kohtanen et al., in preparation).

CONCLUSIONS

This work describes a new approach to measure and characterize guided (Lamb) wave propagation in the human skull using scanning laser Doppler vibrometry. Through the use of ultrasonic transducers and non-contact velocity measurements, guided waves can be directly excited in the skull and measured with improved clarity. By means of the full velocity wavefield measurement, propagating waves can be clearly visualized and characterized using the 2-D FFT, which yields distinct wave dispersion branches. Experimental wavefield measurements and dispersion curves are presented for waves propagating near the squamous suture in the temporal and parietal bones. The skull geometry is obtained using a medical CT scanner, which provides geometric information on the skull cross-section in the plane of the measurement. This information is used to develop a simplified dispersion model by the SAFE method, yielding effective isotropic properties and thickness parameters. These properties can be employed for the assessment of material variations across the skull surface and for the formulation of lowdimensionality finite-element models devoted specifically to the analysis of guided wave propagation. In this context, low dimensionality implies the need not to resolve fully the porosity of the bone structure or other features that are significantly smaller than the range of wavelengths governing guided wave motion. The experimental results suggest that skull geometry will play a key role in the use of guided waves in clinical systems, potentially limiting the viable regions of the skull. Together, these results indicate that the use of scanning laser Doppler vibrometry can provide useful information regarding the properties of skull bone, with the potential to enhance focused ultrasound therapeutics for the brain and enable non-invasive detection of suture anomalies or near-skull brain metastases and hemorrhages. Future efforts may consider the effects of porosity (especially for high frequencies) and the implementation of layered modeling of the cortical tables and the diploë, Lamb wave characterization for different cranial bone regions, as well as the presence of additional layers such as the skin.

Acknowledgments—This material is based on work supported by the National Science Foundation under Grant Nos. 1830577 and 1933158.

Conflict of interest disclosure—The authors have no conflicts of interest to declare.

SUPPLEMENTARY MATERIALS

Supplementary material associated with this article can be found in the online version at doi:10.1016/j.ultra smedbio.2020.11.019.

REFERENCES

- Adams C, McLaughlan J, Nie L, Freear S. Excitation and acquisition of cranial guided waves using a concave array transducer. In: Proceedings of Meetings on Acoustics 173 EAA. Melville, NY30, . : Acoustical Society of America; 2017 055003.
- Alleyne D, Cawley P. A two-dimensional Fourier transform method for the measurement of propagating multimode signals. J Acoust Soc Am 1991;89:1159–1168.
- Aubry JF, Tanter M. MR-guided transcranial focused ultrasound. In: Escoffre JM, Bouakaz A, (eds). Therapeutic ultrasound. Cham: Springer; 2016. p. 97–111.
- Aubry JF, Tanter M, Pernot M, Thomas JL, Fink M. Experimental demonstration of noninvasive transskull adaptive focusing based on prior computed tomography scans. Journal Acoust Soc Am 2003:113:84–93.
- Bochud N, Vallet Q, Minonzio JG, Laugier P. Predicting bone strength with ultrasonic guided waves. Sci Rep 2017;7:43628.
- Boruah S, Subit DL, Paskoff GR, Shender BS, Crandall JR, Salzar RS. Influence of bone microstructure on the mechanical properties of skull cortical bone—A combined experimental and computational approach. J Mech Behav Biomed Mater 2017;65:688–704.
- Clement GT, Hynynen K. A non-invasive method for focusing ultrasound through the human skull. Phys Med Biol 2002;47:1219.
- Clement GT, Sun J, Giesecke T, Hynynen K. A hemisphere array for noninvasive ultrasound brain therapy and surgery. Phys Med Biol 2000;45:3707.
- Datta SK, Shah AH, Bratton R, Chakraborty T. Wave propagation in laminated composite plates. J Acoust Soc Am 1988;83:2020–2026.
- Dayal V, Kinra VK. Leaky lamb waves in an anisotropic plate: I. An exact solution and experiments. J Acoust Soc Am 1989;85:2268– 2276.
- Elias WJ, Huss D, Voss T, Loomba J, Khaled M, Zadicario E, Frysinger RC, Sperling SA, Wylie S, Monteith SJ, Druzgal J, Shah BB. A pilot study of focused ultrasound thalamotomy for essential tremor. N Engl J Med 2013;369:640–648.
- Elias WJ, Lipsman N, Ondo WG, Ghanouni P, Kim YG, Lee W, Schwartz M, Hynynen K, Lozano AM, Shah BB, Huss D, Dallapiazza RF, Gwinn R, Witt J, Ro S, Eisenberg HM, Fishman PS, Gandhi D, Halpern CH, Chuang R, Butts Pauly K, Tierney TS, Hayes MT, Rees Cosgrove G, Yamaguchi T, Abe K, Taira T, Chang JW. A randomized trial of focused ultrasound thalamotomy for essential tremor. N Engl J Med 2016;375:730–739.

- Estrada H, Gottschalk S, Reiss M, Neuschmelting V, Goldbrunner R, Razansky D. Observation of guided acoustic waves in a human skull. Ultrasound Med Biol 2018;44:2388–2392.
- Fearon JA, Singh DJ, Beals SP, Jack CY. The diagnosis and treatment of single-sutural synostoses: Are computed tomographic scans necessary?. Plast Reconstr Surg 2007;120:1327–1331.
- Firouzi K, Ghanouni P, Khuri-Yakub BT. Efficient transcranial ultrasound delivery via excitation of lamb waves: Concept and preliminary results. 2017 IEEE International Ultrasonics Symposium (IUS), Washington, DC. Piscataway, NJ.: IEEE; 2017. p. 1–4.
- Foiret J, Minonzio JG, Chappard C, Talmant M, Laugier P. Combined estimation of thickness and velocities using ultrasound guided waves: A pioneering study on in vitro cortical bone samples. IEEE Trans Ultrason Ferroelectr Freq Control 2014;61:1478–1488.
- Fry FJ, Barger JE. Acoustical properties of the human skull. J Acoust Soc Am 1978;63:1576–1590.
- Hubbard RP. Flexure of layered cranial bone. J Biomech 1971;4:251–263.
- Hynynen K, Clement GT, McDannold N, Vykhodtseva N, King R, White PJ, Vitek S, Jolesz FA. 500-element ultrasound phased array system for noninvasive focal surgery of the brain: A preliminary rabbit study with ex vivo human skulls. Magn Reson Med 2004;52:100–107.
- Hynynen K, McDannold N, Sheikov NA, Jolesz FA, Vykhodtseva N. Local and reversible blood-brain barrier disruption by noninvasive focused ultrasound at frequencies suitable for trans-skull sonications. Neuroimage 2005;24:12–20.
- Jaslow CR. Mechanical properties of cranial sutures. J Biomech 1990;23:313–321.
- Kinoshita M, McDannold N, Jolesz FA, Hynynen K. Noninvasive localized delivery of herceptin to the mouse brain by MRI-guided focused ultrasound-induced blood-brain barrier disruption. Proc Natl Acad Sci USA 2006;103:11719–11723.
- Kohtanen E, Mazzotti M, Ruzzene M, Erturk A. Vibration-based elastic parameter identification of the diploë and cortical tables in dry cranial bones. In preparation.
- Kyriakou A, Neufeld E, Werner B, Paulides MM, Szekely G, Kuster N. A review of numerical and experimental compensation techniques for skull-induced phase aberrations in transcranial focused ultrasound. Int J Hyperthermia 2014;30:36–46.
- Lipsman N, Mainprize TG, Schwartz ML, Hynynen K, Lozano AM. Intracranial applications of magnetic resonance-guided focused ultrasound. Neurotherapeutics 2014;11:593–605.
- Margulies SS, Thibault KL. Infant skull and suture properties: Measurements and implications for mechanisms of pediatric brain injury. J Biomech Eng 2000;122:364–371.
- Mazzotti M, Sugino C, Kohtanen E, Erturk A, Ruzzene M. Experimental identification of high order Lamb waves and estimation of the mechanical properties of a dry human skull. Under review.
- McElhaney JH, Fogle JL, Melvin JW, Haynes RR, Roberts VL, Alem NM. Mechanical properties of cranial bone. J Biomech 1970;3:495–511.
- Mesiwala AH, Farrell L, Wenzel HJ, Silbergeld DL, Crum LA, Winn HR, Mourad PD. High-intensity focused ultrasound selectively disrupts the blood-brain barrier in vivo. Ultrasound Med Biol 2002;28;389–400.
- Michaels TE, Michaels JE, Ruzzene M. Frequency-wavenumber domain analysis of guided wavefields. Ultrasonics 2011;51:452–466.
- Miller GW, Eames M, Snell J, Aubry JF. Ultrashort echo-time MRI versus CT for skull aberration correction in MR-guided transcranial focused ultrasound: In vitro comparison on human calvaria. Med Phys 2015;42:2223–2233.
- Moilanen P. Ultrasonic guided waves in bone. IEEE Trans Ultrason Ferroelectr Freq Control 2008;55:1277–1286.
- Moilanen P, Nicholson PH, Kilappa V, Cheng S, Timonen J. Assessment of the cortical bone thickness using ultrasonic guided waves: Modelling and in vitro study. Ultrasound Med Biol 2007;33:254–262.
- Nicholson PH, Moilanen P, Karkkainen T, Timonen J, Cheng S. Guided ultrasonic waves in long bones: Modelling, experiment and in vivo application. Physiol Meas 2002;23:755–768.
- Niethammer M, Jacobs LJ, Qu J, Jarzynski J. Time—frequency representations of Lamb waves. J Acoust Soc Am 2001;109:1841–1847.

- Odeen H, de Bever J, Almquist S, Farrer A, Todd N, Payne A, Snell JW, Christensen DA, Parker DL. Treatment envelope evaluation in transcranial magnetic resonance-guided focused ultrasound utilizing 3 D MR thermometry. J Ther Ultrasound 2014;2:19.
- Peterson J, Dechow PC. Material properties of the human cranial vault and zygoma. Anat Rec A Discov Mol Cell Evol Biol 2003;274:785–797.
- Protopappas VC, Fotiadis DI, Malizos KN. Guided ultrasound wave propagation in intact and healing long bones. Ultrasound Med Biol 2006;32:693–708.
- Rabiner JE, Friedman LM, Khine H, Avner JR, Tsung JW. Accuracy of point-of-care ultrasound for diagnosis of skull fractures in children. Pediatrics 2013;131:e1757–e1764.
- Regelsberger J, Delling G, Helmke K, Tsokos M, Kammler G, Kranzlein H, Westphal M. Ultrasound in the diagnosis of craniosynostosis. J Craniofac Surg 2006;17:623–625.
- Ruzzene M. Frequency-wavenumber domain filtering for improved damage visualization. Smart Mater Struct 2007;16: 2116

- Tian Z, Yu L. Lamb wave frequency-wavenumber analysis and decomposition. J Intell Mater Syst Struct 2014;25: 1107–1123.
- Vavva MG, Protopappas VC, Gergidis LN, Charalambopoulos A, Fotiadis DI, Polyzos D. The effect of boundary conditions on guided wave propagation in two-dimensional models of healing bone. Ultrasonics 2008;48:598–606.
- Weinberg ER, Tunik MG, Tsung JW. Accuracy of clinician-performed point-of-care ultrasound for the diagnosis of fractures in children and young adults. Injury 2010;41:862–868.
- Wood JL. Dynamic response of human cranial bone. J Biomech 1971:4:1–12.
- Yoganandan N, Pintar FA, Sances A, Jr, Walsh PR, Ewing CL, Thomas DJ, Snyder RG. Biomechanics of skull fracture. J Neurotrauma 1995;12:659–668.
- Zhang X, Fincke JR, Wynn CM, Johnson MR, Haupt RW, Anthony BW. Full noncontact laser ultrasound: First human data. Light Sci Appl 2019;8:1–11.